Modelling delamination migration in angle-ply laminates

B. Y. Chen[a,1,*], T. E. Tay[a], S. T. Pinho[b], V. B. C. Tan[a]

[a]*Department of Mechanical Engineering, National University of Singapore. 9 Engineering Drive 1, Singapore 117575*

[b]*Department of Aeronautics, Imperial College London. London SW7 2AZ, UK*

Abstract

This paper presents a numerical study of the delamination migration in angle-ply laminates observed in experiments reported in the literature, where the delamination originally propagates along the lower, 0°/60° interface and later migrates onto the upper, 60°/0° interface. The recently-developed Floating Node Method (FNM) is used for modelling this problem. The initiation and propagation of both delamination and matrix cracks are modelled within the FNM elements. Experimentally-observed phenomena such as the numerous kinking attempts and the multiple onset locations of migration are successfully predicted. The effect of load offset on the locations of migration is captured. In addition, this work tries to shed light on the proper use of standard cohesive elements in cases where delamination migration is expected.

Keywords:

Delamination migration; computational modelling; cohesive element; floating node method

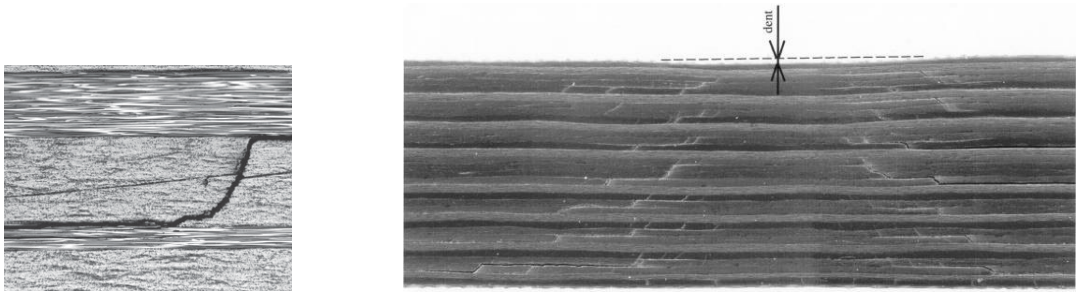
1. Introduction

Delamination is one of the most critical failure mechanisms in composite laminates. While delamination usually initiates on an interface between two dissimilar plies, its propagation is often complicated by delamination migration, i.e., the phenomenon of delamination

*Corresponding author

Email address: boyang.chen.cn@gmail.com (B. Y. Chen)

[1]Tel: +65 90286157. Address: Block EA, # 02-21, 9 Engineering Drive 1, Singapore 117575



(a) Delamination migration [1]. (b) Delamination migrations in low-velocity impact [2].

Figure 1: Delamination migration in composites.

initially propagating along one interface and later jumping onto another through a matrix crack (see Figure 1a) [1]. This is particularly pertinent in the case of low-velocity impact (see Figure 1b) [2].

Considerable experimental research has been dedicated to the study of delamination migration [1, 3–7]. In particular, Ratcliffe et al. [1, 6] designed an experiment to isolate the entire process of a single delamination migration event and examined its driving mechanisms in cross-ply tape laminates (Figure 2 with $\theta = 90°$). In their experiments, the delamination propagated along the lower, $0°/90°$ interface until a single, through-the-width matrix crack in the $90°$ plies caused the migration of the delamination onto the upper, $90°/0°$ interface. In addition, the effect of the load offset with respect to the crack tip location (i.e., the value of L/a_0 in Figure 2) was examined. It is found that this offset determines the initial shear sign in front of the crack tip and dictates the eventual location of delamination migration [1]. Since then, several modelling works have been reported to study the delamination migration in cross-ply tape laminates using different modelling methods [8–11].

The laminates in actual structures are rarely cross-ply ones. Promising results have been obtained on the study of delamination migration in angle-ply laminates using the XFEM-CE method (a method combining the extended finite element method (XFEM) with cohesive element (CE) [12]), where migration starts right from the tip of the pre-crack and is accomplished by a continuous matrix crack across the ply width [12, 13]. Recently, the

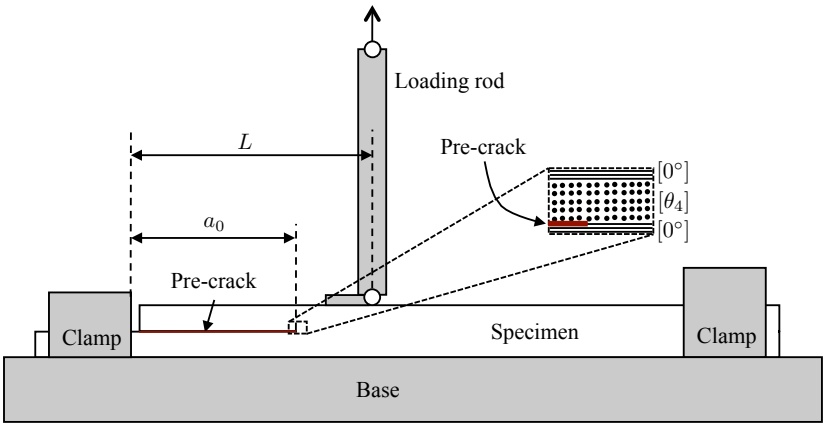


Figure 2: The setup of the delamination migration experiments by Ratcliffe et al. [1, 7] (not drawn to scale).

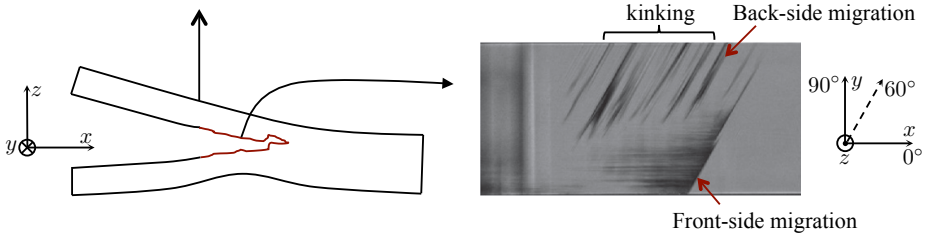


Figure 3: The X-Ray image of the upper arm of a specimen with a 0°/60° migration interface [7].

experimental setup in [1, 6] has been adopted to investigate delamination migration in more generic angle-ply laminates in [7]. It is found that the migration processes can be more complicated than those in the simpler cross-ply laminates in [1, 6] and the angle-ply ones in [12, 13]. Figure 3 shows the X-Ray image of the upper arm of a specimen from Pernice et al. [7] with $\theta = 60°$. Firstly, many kinking events (defined as the turning of delamination into the 60° ply [7]) are observed prior to the eventual migration. Secondly, the migration cannot be represented by a single matrix crack in the 60° ply; instead, it is represented by multiple matrix cracks across the width of the 60° ply.

To the authors' knowledge, the complex migration characteristics of angle-ply laminates observed by Pernice et al. [7], i.e., multiple kinking events before the eventual migration and different migration locations across the specimen width, have yet to be predicted by numerical modelling. Recently, a Floating Node Method (FNM) [8, 14, 15] has been devel-

oped to model complex cracking patterns in composites. It has origins from the Hansbo's method [16] and its variants [17–22]. When it comes to modelling crack propagations, the above-mentioned methods, together with many others such as the meshless methods [23–27], the XFEM-based methods [12, 28–33], the phase-field method [34–37] and the thick level-set method [38–41], all belong to the broad family of methods which do not rely on remeshing. This paper presents the modelling of the above-mentioned delamination migration phenomena, using the FNM. The effect of the load offset (i.e., L/a_0 in Figure 2) is also examined. This work also tries to shed light on the immediate applicability of the standard cohesive elements (which have been so successfully used for the modelling of delamination [42–52]) for the modelling of delamination migration.

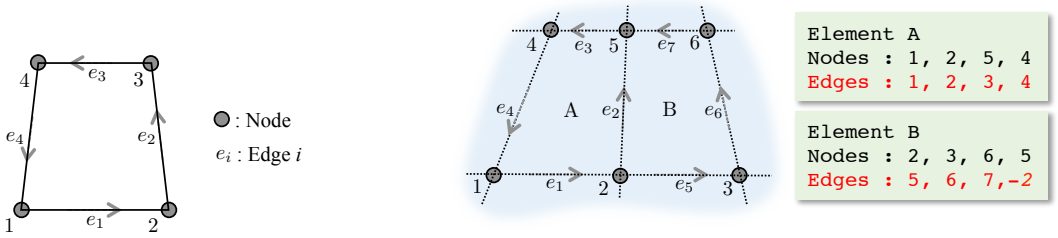
The structure of the paper is organised as follows. The background of the FNM is presented in Section 2, followed by the finite element model in Section 3 and the results in Section 4. Discussions of the results are presented in Section 5, and finally the conclusions are drawn in Section 6.

2. Background of the Floating Node Method for composites

The full details of the FNM for composite laminates can be found in [15]. This section presents the essential aspects of the method for the understanding of its application in this paper.

2.1. Edge connectivity and floating DoF

In the FNM, the definition of an element is enriched to include both node connectivity and edge connectivity, where the global indices of the nodes and edges of an element are recorded according to an ordered convention (Figure 4a and 4b). In addition to allocating DoFs to the nodes, DoFs are also allocated to the edges (and, in general, to element entities such as surfaces and volumes). In contrast to the nodal DoFs, the DoFs of edges are called



(a) Definition of an element in FNM: nodes and edges.

(b) A FNM mesh and element connectivities.

Figure 4: Edge connectivity and floating DoF.

floating DoFs. Floating DoFs can be freely allocated to any geometrical entity, and be used to represent the DoF of an arbitrary node on this entity, the location of which may not be known a priori. Details of the 2D FNM elements for the modelling of matrix crack/delamination interaction problems can be found in [8, 14], and those of the 3D FNM for the modelling in-plane tensile failure of composites in [15].

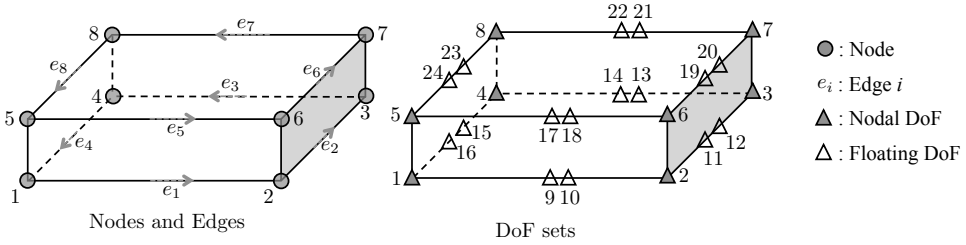
2.2. Ply element

A ply element can be constructed with the FNM, such that a matrix crack can be modelled within its domain. Figure 5a shows the node, edge and DoF definitions of this element. In this paper, matrix cracks are approximated to be vertical.

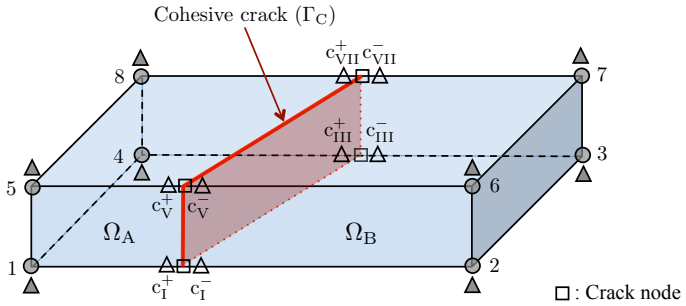
Before matrix cracking, the static equilibrium of a body with volume Ω under body forces with density $\mathbf{f}$ (acting on Ω) and traction $\mathbf{t}$ acting on the boundary Γ_t can be expressed in the weak form as:

$$\int_{\Omega} \boldsymbol{\epsilon}^{\mathrm{T}}(\mathbf{v})\, \boldsymbol{\sigma}\,(\mathbf{u})\ \mathrm{d}\Omega = \int_{\Omega} \mathbf{v}^{\mathrm{T}}\mathbf{f}\,\mathrm{d}\Omega + \int_{\Gamma_t} \mathbf{v}^{\mathrm{T}}\mathbf{t}\,\mathrm{d}\Gamma \tag{1}$$

where $\mathbf{u}$ is the displacement solution, $\mathbf{v}$ is the test function, $\boldsymbol{\epsilon}$ is the strain tensor (related to $\mathbf{u}$ through the differential operator relative to Cartesian coordinates $\mathcal{L}_{\mathbf{x}}$ as $\boldsymbol{\epsilon} = \mathcal{L}_{\mathbf{x}}(\mathbf{u})$), and $\boldsymbol{\sigma}$ is the stress tensor (related to the strains through Hooke's law as $\boldsymbol{\sigma} = \mathbf{D}\boldsymbol{\epsilon}$, with $\mathbf{D}$ being the constitutive tensor). In this case (i.e., before matrix cracking), the ply element is simply a standard linear brick element. The crack nodes do not exist yet, and the floating DoFs



(a) The definitions of a FNM ply element.



(b) A matrix crack introduces four pairs of coinciding crack nodes on four edges of the element.

Figure 5: A partitionable ply element by FNM.

are not used [15]. In the current implementation of the method as user-defined elements of the commercial software Abaqus, the stiffness terms of the unused floating DoFs are all set to zero. Note that the Abaqus solver is able to remove these zero rows and columns from the global stiffness matrix, hence the unused floating DoFs effectively do not play a part in the solution process.

If a certain failure criterion or propagation criterion is met, then a matrix crack initiates or propagates (respectively) within the element domain. Assuming that the matrix crack is a cohesive crack, the weak form of the equilibrium equation now becomes:

$$\int_{\Omega_A \cup \Omega_B} \boldsymbol{\epsilon}^{\mathrm{T}}(\mathbf{v})\, \boldsymbol{\sigma}\,(\mathbf{u})\, \mathrm{d}\Omega + \int_{\Gamma_C} [\![\mathbf{v}]\!]^{\mathrm{T}} \boldsymbol{\tau}_c([\![\mathbf{u}]\!])\, \mathrm{d}\Gamma = \int_{\Omega_A \cup \Omega_B} \mathbf{v}^{\mathrm{T}} \mathbf{f}\, \mathrm{d}\Omega + \int_{\Gamma_t} \mathbf{v}^{\mathrm{T}} \mathbf{t}\, \mathrm{d}\Gamma \qquad (2)$$

where $[\![\bullet]\!]$ represents the jump of a variable between the top and bottom surfaces of the cohesive crack, and $\boldsymbol{\tau}_c$ is the traction acting between the surfaces of the cohesive crack. $\boldsymbol{\tau}_c$ relates to the separation of the top and bottom surfaces of the cohesive crack, $[\![\mathbf{u}]\!]$, through

a constitutive relationship of the form:

$$\boldsymbol{\tau}_{\mathrm{c}} = \mathbf{D}_{\mathrm{CE}} [\![\mathbf{u}]\!] \tag{3}$$

where $\mathbf{D}_{\mathrm{CE}}$ is the cohesive constitutive tensor.

Supposing that the matrix crack cuts across four edges of the element, for instance, Edge 1, Edge 3, Edge 5 and Edge 7, then it creates four pairs of initially coinciding crack nodes, $c_{\mathrm{I}}^{\pm}$, $c_{\mathrm{III}}^{\pm}$, $c_{\mathrm{V}}^{\pm}$ and $c_{\mathrm{VII}}^{\pm}$, on the four edges, respectively (Figure 5b). The coordinates of the crack nodes are the intersections of the crack and the edges. The matrix crack partitions the original domain Ω into two subdomains, Ω_{A} and Ω_{B}, with Γ_{C} being the crack interface. Three Sub-Elements (SEs) can be formed, such that they represent the two bulk subdomains Ω_{A} and Ω_{B} and the cohesive crack Γ_{C}. Note that the nodal coordinates of these SEs are fully defined by the original nodes and crack nodes [15]. With the floating DoF sets allocated to represent the displacements of the crack nodes, the DoF vectors (i.e., $\mathbf{q}_{\Omega_{\mathrm{A}}}, \mathbf{q}_{\Omega_{\mathrm{B}}}, \mathbf{q}_{\Gamma_{\mathrm{C}}}$) of the three SEs are also fully defined. Under the assumption of isoparametric representation, the displacement solution is:

$$\mathbf{u}(\mathbf{x}) = \begin{cases} \mathbf{N}_{\Omega_{\mathrm{A}}}(\mathbf{x})\, \mathbf{q}_{\Omega_{\mathrm{A}}}, & \text{if } \mathbf{x} \in \Omega_{\mathrm{A}}; \\ \mathbf{N}_{\Omega_{\mathrm{B}}}(\mathbf{x})\, \mathbf{q}_{\Omega_{\mathrm{B}}}, & \text{if } \mathbf{x} \in \Omega_{\mathrm{B}}, \end{cases} \tag{4}$$

with

$$[\![\mathbf{u}]\!](\mathbf{x}) = \mathbf{N}_{\Gamma_{\mathrm{C}}}(\mathbf{x})\, \mathbf{q}_{\Gamma_{\mathrm{C}}}, \text{ if } \mathbf{x} \in \Gamma_{\mathrm{C}}, \tag{5}$$

where $\mathbf{N}_{\Omega_{\mathrm{A}}}$, $\mathbf{N}_{\Omega_{\mathrm{B}}}$ and $\mathbf{N}_{\Gamma_{\mathrm{C}}}$ are the standard finite element shape function matrices (in physical coordinates) of the elements defined by Ω_{A}, Ω_{B} and Γ_{C}, respectively. The stiffness matrices (i.e., $\mathbf{K}_{\Omega_{\mathrm{A}}}$, $\mathbf{K}_{\Omega_{\mathrm{B}}}$, $\mathbf{K}_{\Gamma_{\mathrm{C}}}$) and force vectors (i.e., $\mathbf{Q}_{\Omega_{\mathrm{A}}}$, $\mathbf{Q}_{\Omega_{\mathrm{B}}}$, $\mathbf{Q}_{\Gamma_{\mathrm{C}}}$) of the SEs can be calculated using standard finite element integration techniques [15]. The weak form of the

equilibrium equation, Equation (2), can be written in an assembled form as:

$$\mathbf{K}_{\text{el}}\,\mathbf{q}_{\text{el}} = \mathbf{Q}_{\text{el}} \tag{6}$$

with:

$$\begin{aligned} \mathbf{K}_{\text{el}} &= \mathcal{A}\left(\mathbf{K}_{\Omega_{\text{A}}}, \mathbf{K}_{\Omega_{\text{B}}}, \mathbf{K}_{\Gamma_{\text{C}}}\right), \\ \mathbf{q}_{\text{el}} &= \mathcal{A}\left(\mathbf{q}_{\Omega_{\text{A}}}, \mathbf{q}_{\Omega_{\text{B}}}, \mathbf{q}_{\Gamma_{\text{C}}}\right), \\ \mathbf{Q}_{\text{el}} &= \mathcal{A}\left(\mathbf{Q}_{\Omega_{\text{A}}}, \mathbf{Q}_{\Omega_{\text{B}}}, \mathbf{Q}_{\Gamma_{\text{C}}}\right), \end{aligned} \tag{7}$$

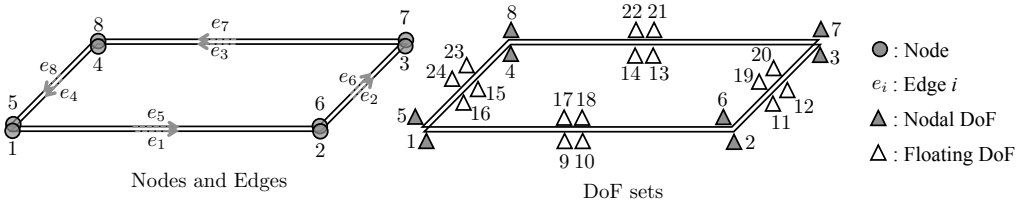
where $\mathcal{A}$ is the assembly operator.

2.3. Cohesive element

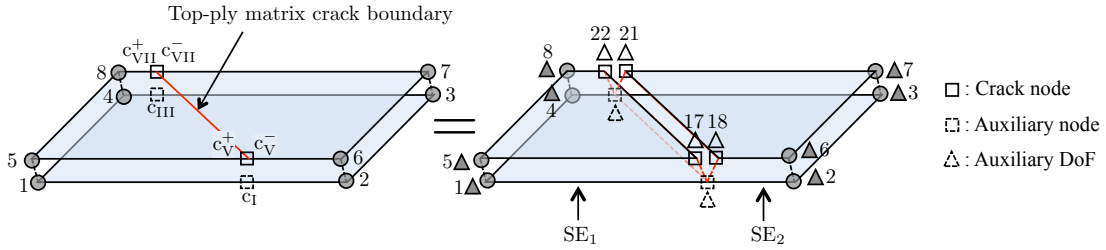
Previous studies have shown that the explicit modelling of matrix crack boundaries on the interfaces is needed for the accurate prediction of matrix crack/delamination interaction [14, 22]. In 3D laminates, matrix cracks may occur on both sides of the interface. In order to capture the stress concentrations induced by both matrix cracks, a partitionable cohesive element is formulated. It consists of two initially coinciding surfaces, with suitable connectivities for both its nodes and its edges. A pair of floating DoF sets are allocated to each edge of the element (Figure 6a).

Before any matrix crack appearing from the top or bottom ply element, the cohesive element is a standard 8-node linear cohesive element and the floating DoFs are not used.

If a matrix crack occurs on the top ply element (Figure 6b), then it creates two pairs of initially coinciding crack nodes on these edges, i.e., $c_{\text{V}}^{\pm}$ and $c_{\text{VII}}^{\pm}$, respectively. Two auxiliary nodes which initially coincide with the crack nodes can also be defined and located on the bottom surface of the cohesive element, ie., c_{I} and c_{III}. These nodes allow the nodal coordinates of the SEs, in this case SE_1 and SE_2 (see Figure 6b), to be defined. With the



(a) The definitions of a FNM cohesive element.



(b) The FNM cohesive element can be partitioned with respect to a matrix crack from a neighbouring ply.

Figure 6: A partitionable cohesive element by the FNM.

use of the floating DoFs, the DoF vectors (i.e., $\mathbf{q}_{\mathrm{SE}_1}, \mathbf{q}_{\mathrm{SE}_2}$) of the two SEs can be formed. The separation at location $\mathbf{x}$, $[\![\mathbf{u}]\!](\mathbf{x})$, is:

$$[\![\mathbf{u}]\!](\mathbf{x}) = \begin{cases} \mathbf{N}_{\mathrm{SE}_1}(\mathbf{x})\,\mathbf{q}_{\mathrm{SE}_1}, & \text{if } \mathbf{x} \in \Omega_{\mathrm{SE}_1}, \\ \mathbf{N}_{\mathrm{SE}_2}(\mathbf{x})\,\mathbf{q}_{\mathrm{SE}_2}, & \text{if } \mathbf{x} \in \Omega_{\mathrm{SE}_2}, \end{cases} \tag{8}$$

where $\mathbf{N}_{\mathrm{SE}_1}$ and $\mathbf{N}_{\mathrm{SE}_2}$ are shape function matrices (in physical coordinates) of the cohesive SEs on SE_1 and SE_2, respectively. The stiffness matrices of the two SEs, $\mathbf{K}_{\mathrm{SE}_1}$ and $\mathbf{K}_{\mathrm{SE}_2}$, can be calculated using the standard procedure detailed in [15, 42]. The overall stiffness matrix of the cohesive element, $\mathbf{K}_{\mathrm{CE}}$, is obtained from the assembly of those of the two SEs:

$$\mathbf{K}_{\mathrm{CE}} = \mathcal{A}\left(\mathbf{K}_{\mathrm{SE}_1}, \quad \mathbf{K}_{\mathrm{SE}_2}\right). \tag{9}$$

Similarly, if a matrix crack occurs on the bottom ply element, the element can be partitioned and integrated using the same procedure above, where the floating DoFs on the bottom edges would be utilized to form the SEs accordingly. Simultaneous matrix cracks

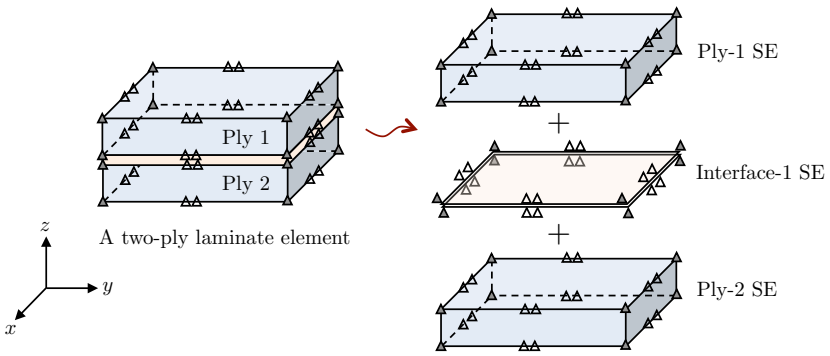


Figure 7: A laminate element can be constructed based on layup.

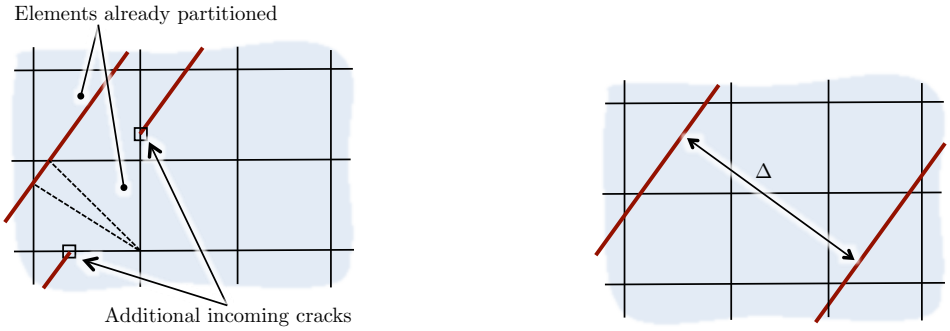
on top and bottom ply elements can be represented with suitable floating DoFs and corresponding partitions. This is however not relevant in this study, as the migration process involves the matrix cracks only in the middle 60° ply-block.

2.4. Laminate element

With the ply and cohesive elements defined in the previous sections, a laminate element can be formed, such that ply and cohesive elements are SEs of the laminate element (Figure 7). The definition of connectivities of the SEs is detailed in [15] and it is omitted here for brevity. Note that all the SEs are within the same laminate element, facilitating the exchange of information between different SEs. In addition, the use of such a laminate element greatly reduces the effort of preprocessing. The layup and ply thickness are defining parameters of this element, and they do not need to be reflected in the mesh.

2.5. Crack propagation

With the edge connectivity available for each element, an edge status variable approach is developed for the modelling of cohesive crack propagations in FNM. A list of all the edges is created, where a status variable, μ, and a coordinates vector, $\mathbf{x}_c$, are allocated to every edge. μ stores the current status of the edge, i.e., intact, hosting a crack tip, or already at the wake of the crack tip. $\mathbf{x}_c$ stores the coordinates of the crack node on the edge. An element only needs to read a fixed amount of information to propagate a crack, i.e., the



(a) Arrest of additional cracks on edges of partitioned elements [15].

(b) A minimum spacing of Δ between cracks.

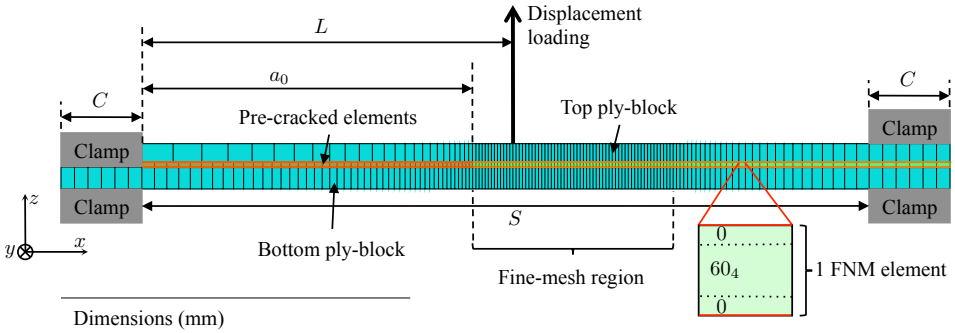
Figure 8: A mininum spacing between matrix cracks ensures the continuity of crack propagations.

edge status variables of its own edges, regardless of the total number of cracks in the mesh. Details of this can be found in [15].

After a crack has crossed an element and the element has been partitioned, neighbouring cracks may again reach the boundary of the element (see Figure 8a). Ideally, the finite element mesh should be fine enough such that intact elements always exist between every two matrix cracks (i.e., the stress field and the strain energy between two existing matrix cracks are insufficient to drive a new matrix crack between them [14]), and the situation in Figure 8a should not occur. In this work, the situation in Figure 8a is numerically eliminated by setting a minimum spacing parameter (Δ) between two neighbouring matrix cracks (see 8b). Δ should be just large enough to avoid the situation in Figure 8a and small enough so that a reasonable density of matrix cracks could still be represented. In this study, Δ is set to be twice the typical element size in the mesh.

2.6. Failure theories

Since the problem of this study contains only matrix failure and delamination, the choice of fibre failure theory is irrelevant. The matrix failure onset is determined by the quadratic interactive criterion based on the normal and shear tractions on the matrix crack surface. Once the matrix failure onset occurs, the element is partitioned such that a cohesive SE



Dimensions (mm)				
a_0	S	C	h^*	B^{**}
53	114.3	12.7	0.127	12.7

$^*h$: ply thickness

$^{**}B$: specimen width

Layups	
Top ply-block:	$[-60_4/-30/-60/-30/90/-30/30/90/30/60/30/60_4/0/-60_4]$
FNM element:	$[0/\mathrm{T}/60_4/0]$
Bottom ply-block:	$[60/0/60_3/-60_4/-30/-60/-30/90/-30/30/90/30/60/30/60_4/-60_4]$

T: location of pre-crack

Figure 9: Finite element model of the migration experiment in Figure 2.

models the cohesive crack in the element domain, as detailed in Section 2.2. The failure onset of this cohesive SE is determined by the same quadratic interactive criterion as the one for matrix failure onset. The damage evolution of the cohesive SE follows a mixed-mode (power-law) bilinear cohesive law.

Similarly to matrix cracking, delamination onset in the cohesive elements and SEs is determined by the same quadratic interactive criterion as the one for matrix failure onset. The damage evolution in delamination also follows the same mixed-mode (power-law) bilinear cohesive law as the one for matrix damage evolution.

Note that no specific criterion for delamination migration is used in this work. Delamination migration, if predicted, would be the result of the joining of a matrix crack with delamination.

3. Finite Element Model

The finite element model of the migration experiment in Figure 2 is built in the commercial finite element software Abaqus. It is depicted in Figure 9. The model is composed of three parts, i.e., a middle ply-block (of layup $[0/\mathrm{T}/60_4/0]$, 'T' denotes the pre-crack) within which the entire migration event occurs, and two supporting ply-blocks above and below the middle ply-block. The two supporting ply-blocks are each modelled within a single layer of reduced-integration solid elements using the classical lamination theory. No damage or failure is considered in the supporting ply-blocks. The middle ply-block is modelled with a single layer of FNM laminate element (see Section 2.4), implemented as a user-defined element. The three parts are joined together using tie constraints. The clamping boundary conditions are modelled using the approach in [8], where the clamps are explicitly modelled (here as rigid bodies) and frictional contacts (assuming Coulomb's law, with a coefficient of friction of 0.23 [8]) are defined between the clamps and the specimen (see more details in [8]). The element size is 0.5 mm $\times$ 0.5 mm in the fine-mesh region in Figure 9. The material properties and parameters used in the model are summarized in Table 1. The analysis method is implicit, with non-default solver control parameters to achieve convergence (see details in the appendix of ref. [15]).

4. Results

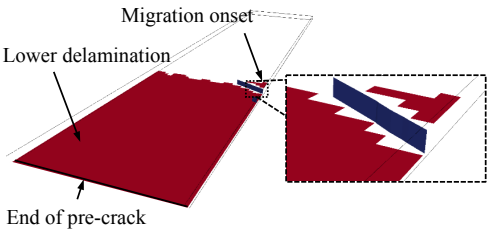
4.1. Baseline case: $L/a_0 = 1$

The experiments in [7] showed results for different L/a_0 ratios. The predictions for the baseline case, i.e., $L/a_0 = 1$, are presented in this section. The predicted failure patterns are shown in Figure 10. The post-processing is done with the open-source visualisation software ParaView. The blue-coloured strips represent matrix cracks in the ply elements, and the red-coloured regions represent delamination on the interface. d is the damage variable of the cohesive law, defined as the percentage of the stiffness degradation (i.e.,

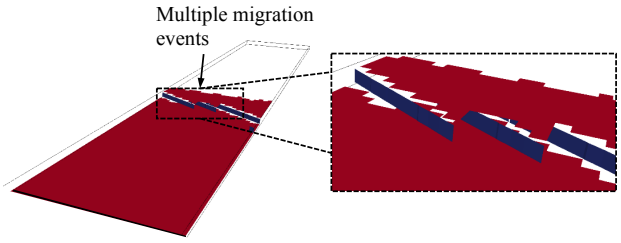
Table 1: Material properties & parameters used in the finite element model[7, 8].

Property	Value
Longitudinal Young's modulus: E_1 (GPa)	161
Transverse Young's modulus: E_2, E_3 (GPa)	11.38
Shear modulus: G_{12}, G_{13} (GPa)	5.17
Shear modulus: G_{23} (GPa)	3.98
Poisson's ratio: ν_{12}, ν_{13}	0.32
Poisson's ratio: ν_{23}	0.44
Transverse tensile strength: $\tau_{\mathrm{n}}^{\mathrm{c}}$ (MPa)	60
Intralaminar shear strength: $\tau_{\mathrm{t}}^{\mathrm{c}}, \tau_{\ell}^{\mathrm{c}}$ (MPa)	90
Interfacial normal strength: $\tau_{\mathrm{n}}^{\mathrm{c}}$ (MPa)	60
Interfacial shear strength: $\tau_{\mathrm{t}}^{\mathrm{c}}, \tau_{\ell}^{\mathrm{c}}$ (MPa)	90
Mode I matrix/interfacial fracture toughness: G_{nc} (kJ/m^2)	0.21
Mode II matrix/interfacial fracture toughness: $G_{\mathrm{tc}}, G_{\ell \mathrm{c}}$ (kJ/m^2)	0.77
Power-law exponent for mixed-mode fracture: α	1 (assumed)
Penalty stiffness of cohesive elements: $K_{\mathrm{n}}, K_{\ell}, K_{\mathrm{t}}$ (N/mm^3)	1.6×10^5 [46]
Minimum crack spacing: Δ (mm)	1

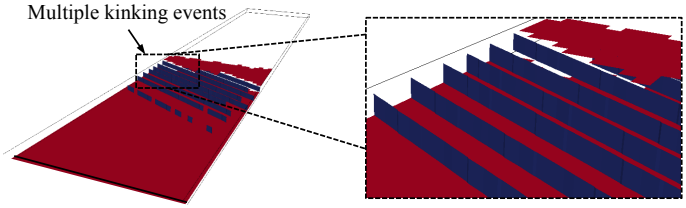
$d = 1$ represents total failure and $d > 0$ represents damage onset in the cohesive element). d_{matrix} is the damage variable for the cohesive elements representing matrix cracks (i.e., the cohesive SEs of partitioned ply elements in Section 2.2), and d_{interf} is that for the cohesive elements on the interface. The partitions of the cohesive elements on the interface (i.e., Figure 6b) are not explicitly plotted and the original element geometry with the average d_{interf} of their SEs are shown, hence the staggered delamination fronts in Figure 10. It can be seen that delamination originally propagates along the lower, pre-cracked interface (Figure 10a), and then migrates onto the upper interface through multiple matrix cracks across the width of the laminate (Figure 10b). In addition, the matrix damage patterns with non-zero damage variables (i.e., $d_{\mathrm{matrix}} > 0$) clearly show numerous kinking attempts before the final occurrence of migration. The predicted delamination and matrix damage patterns are compared against the experimental X-Ray image in Figure 11a. The predicted patterns show a similar amount of kinking events as that in the X-Ray image, and the relative position between the front and rear side migrations (denoted by 'F' and 'R' respectively) are well



(a) Failure patterns ($d_{\text{matrix}} = 1$, $d_{\text{interf}} = 1$) show onset of delamination migration.



(b) Failure patterns ($d_{\text{matrix}} = 1$, $d_{\text{interf}} = 1$) show complete migration across the width (by multiple matrix cracks) at the end of loading.



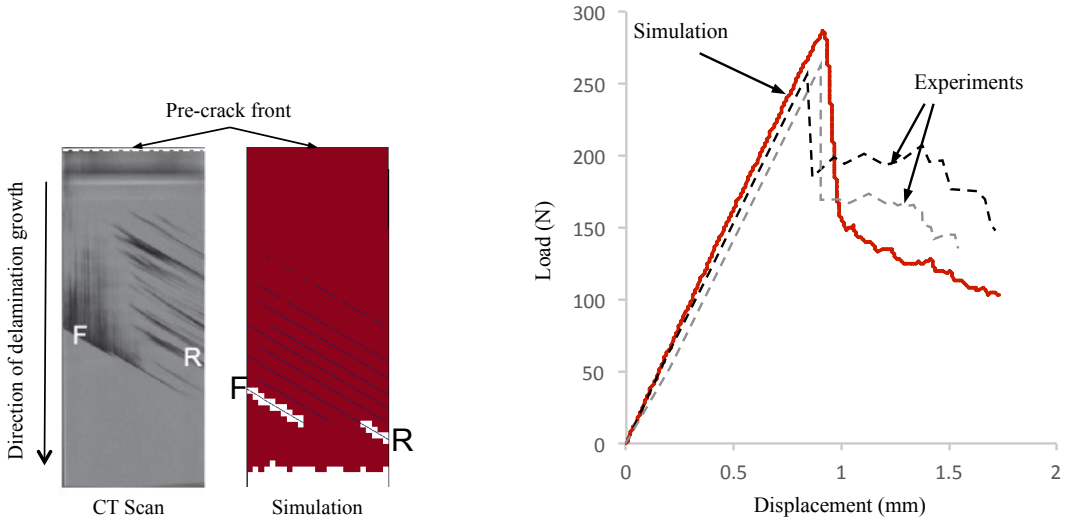
(c) Matrix damage patterns with $d_{\text{matrix}} > 0$ reveal numerous kinking attempts before eventual migration ($d_{\text{interf}} = 1$).

Figure 10: Simulation results of the baseline case $L/a_0 = 1$.

predicted. However, the exact locations of migration on the two sides of the laminate are predicted only reasonably, i.e., they are predicted to be slightly further away from the pre-crack than those in the experiments. The predicted load-displacement curve is compared against the experimental curve in [7] in Figure 11b. The predicted stiffness and ultimate load are in good agreement with the experimental ones. The load-drop is predicted to be caused by the failure of many cohesive elements on the lower interface in a few increments, which corresponds well to the unstable propagation of delamination observed in the experiment [7]. The part of the curve after the load-drop is slightly under-predicted by the model.

4.2. Cases with different load offsets

In this section, the results for two cases with different load offsets, i.e., $L/a_0 = 0.35$ and $L/a_0 = 1.1$ respectively, are presented. The predicted patterns are compared against X-Ray images in Figure 12. The effect of the different load offsets is predicted, where a

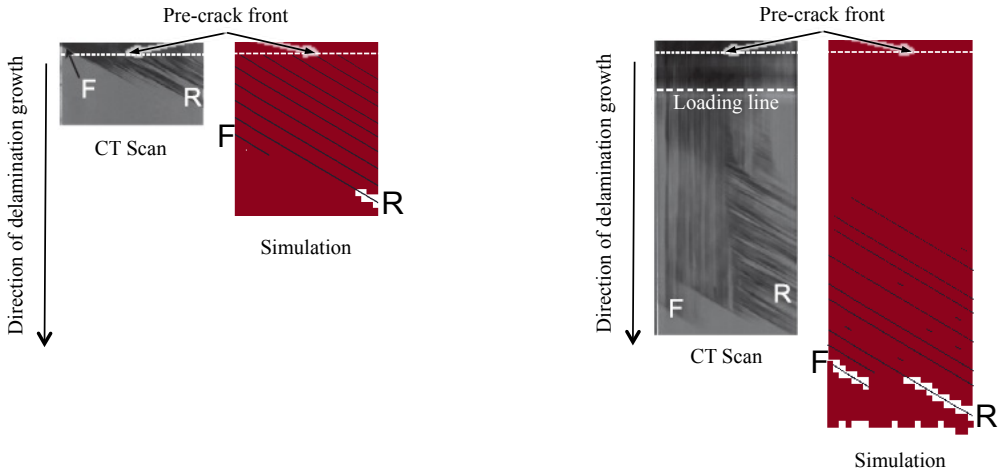


(a) X-Ray image [7] vs. simulated patterns ($d_{\text{matrix}} > 0$, $d_{\text{interf}} = 1$); 'F' and 'R' denote the locations of migration on the front and rear sides of the laminate, respectively.

(b) Predicted load-displacement curve vs. the experimental curve [7].

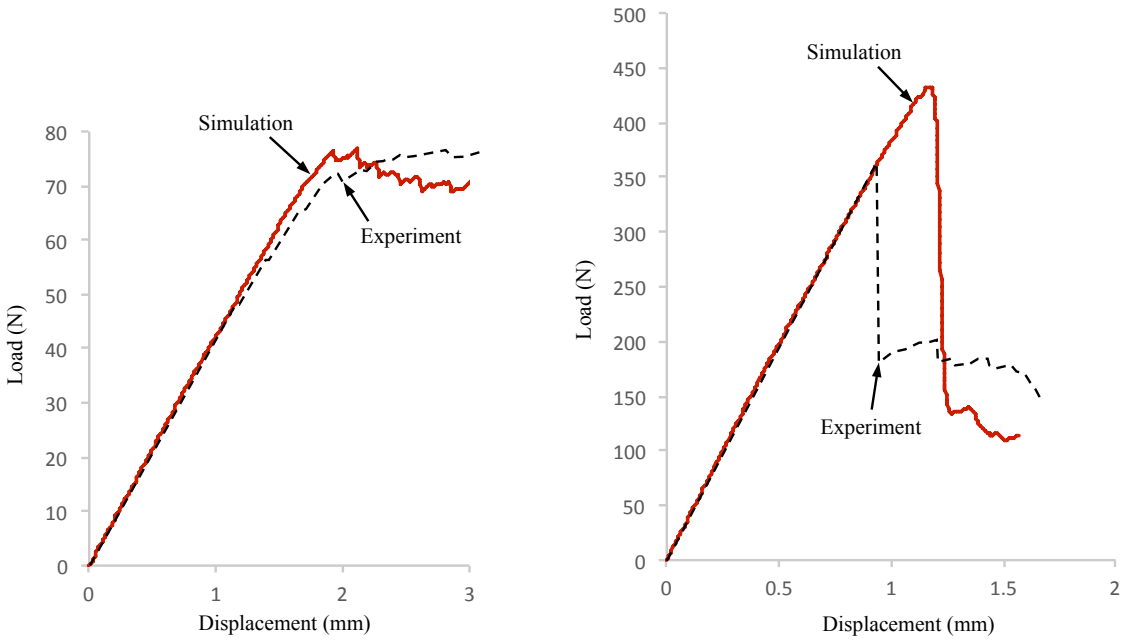
Figure 11: Baseline simulation vs. experiment.

larger L/a_0 leads to longer delamination propagation and a more delayed migration onset. This compares favorably to the experimental observation in [7]. Similarly as in the baseline case, the migration is predicted to be caused by different matrix cracks across the width of the laminate, and the exact locations of migration are all predicted to be further away from the pre-crack front than those in the X-Ray images. The predicted load-displacement curves of the two cases are compared against the experimental ones in Figure 13. In the case of $L/a_0 = 0.35$, good agreement is obtained on both the stiffness and the ultimate load. In the case of $L/a_0 = 1.1$, the stiffness is accurately predicted, but the ultimate load is over-predicted by approximately 21%. The sharp load-drop is caused by the simultaneous failure of a large number of cohesive elements on the lower interface. This agrees well with the experimental observation of the unstable propagation of delamination [7]. In both cases, and similarly as in the baseline case, the post load-drop parts of the curves are slightly under-predicted.



(a) Case $L/a_0 = 0.35$ (b) Case $L/a_0 = 1.1$

Figure 12: X-Ray images [7] vs. simulated patterns ($d_{\text{matrix}} > 0$, $d_{\text{interf}} = 1$); 'F' and 'R' denote the locations of migration on the front and rear sides of the laminate, respectively.



(a) Case $L/a_0 = 0.35$ (b) Case $L/a_0 = 1.1$

Figure 13: Predicted load-displacement curves vs. experimental ones [7].

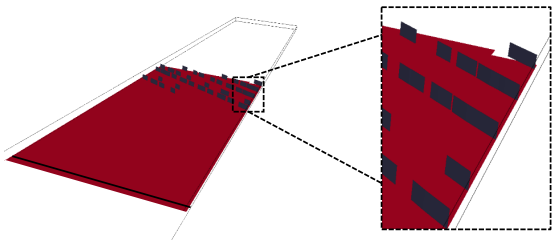


Figure 14: Final failure patterns ($d_{\text{matrix}} = 1$, $d_{\text{interf}} = 1$) of the baseline case with standard, unpartitioned cohesive elements on the interface (see Figure 10b for comparison).

4.3. Baseline case with standard cohesive elements on the interface

In this section, the baseline case in Section 4.1 is revisited. Instead of using the partitionable cohesive elements in Section 2.3 on the interface, standard cohesive elements are used for the modelling of delamination. In other words, the partition of the cohesive element with respect to matrix cracks (see Figure 6b) is suppressed to investigate its importance for the prediction of delamination migration. The predicted failure patterns are shown in Figure 14. It can be seen that despite the multiple events of kinking, delamination remains on the lower interface without migration throughout the course of loading.

5. Discussion

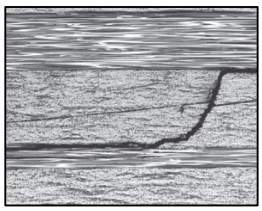
The predicted results in Section 4.1 and Section 4.2 are in good agreement with the experimental results, capturing the complexity of the migration process in angle-ply laminates observed experimentally by Pernice et al. [7]. However, the results show that the predicted migration events appear slightly later in the course of delamination than those in the experiments [7] (see Figure 11a and Figure 12). There could be several reasons for this slight difference. Firstly, delamination migration is modelled here as the coalescence of failed cohesive SEs in the ply and those on the interfaces, joining together naturally in a stair-case pattern. No specific migration criterion is employed at the delamination front. A more accurate approach would be to calculate precisely the energy release rates at the delamination front along different potential fracture paths and determine the one with the

least resistance, as done in [8]. In addition, the kinking matrix crack in the migration is here approximated by a vertical cohesive SE. A more accurate approach would be to model this kinking matrix crack as a series of inclined matrix cracks, propagating gradually from the lower interface to the upper interface in a curved manner as done in [8]. However, implementing the accurate evaluation of energy release rates at the delamination front and propagating the kinking crack incrementally in a curved geometry, without comprimising the generality of the method for generic loading conditions, is non-trivial.

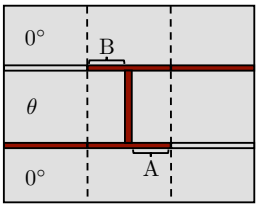
In the predicted load-displacement curves in Figure 11b and Figure 13, the post load-drop curves are slightly under-predicted by the model. Although this part of the curve is generally of little practical interest, it does however correlate to the experimental observation that a significant amount of fibre-bridging exists along with the delamination [7]. As the toughening mechanism of fibre-bridging is not considered in the cohesive laws for delamination, the model under-predicts the residual response of the laminate after the load-drop. Note that the neglect of fibre-bridging in the model could also contribute to the slightly delayed migration onset in the simulation, as a toughened lower interface would have made the migration path relatively more favourable for fracture.

In the case of $L/a_0 = 1.1$ in Section 4.2, the predicted ultimate load is 21% higher than the experimental one (see Figure 13b), while such an over-prediction is not observed on the other two cases (ref Figure 11b and Figure 13a). This could be due to the relatively coarse mesh in the thickness direction of the finite element model (Figure 9), which is insufficient to represent the more complicated stress field through the thickness direction in the case of $L/a_0 = 1.1$ than in the cases of $L/a_0 = 0.35$ (i.e., a modified double-cantilever-beam bending) and $L/a_0 = 1$ (i.e., Mode I loading on pre-crack tip). A more accurate prediction could be obtained through mesh refinement in the thickness direction. However, such a refinement would come with a greatly increased computational cost.

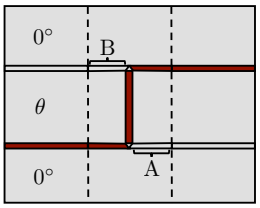
In Section 4.3, the model with standard cohesive elements on the interface is used to



(a) Experimental image of the migration [1].



(b) Modelling of the migration with standard cohesive elements on the interface.



(c) Modelling of the migration with partitioned cohesive elements on the interface.

Figure 15: Difference between standard cohesive element and FNM cohesive element on the modelling of migration: standard cohesive elements introduce artificial crack tips on the regions marked with 'A' and 'B' (red color indicates failure of elements).

simulate the problem in Section 4.1. It fails to predict the occurrence of delamination migration, despite the appearance of several totally-failed kinking cracks in the simulation. This result confirms the previous finding that standard cohesive elements on the interface cannot model accurately the interplay between delamination and matrix cracking [14, 22]. It demonstrates that partitioning the cohesive element with respect to matrix cracks (see Figure 6b) is the determing factor in predicting the phenomenon of delamination migration. Figure 15 illustrates the difference between the standard cohesive elements and the FNM cohesive elements on the modelling of delamination migration. The standard cohesive elements, once failed, would introduce artificial crack tips on the regions marked with 'A' and 'B' (Figure 15b). The artefact at 'A' could cause the delamination to continue on the lower interface without migration (as it is seen in Section 4.3), and that at 'B' could lead the upper delamination to propagate towards the wrong direction. These artefacts are mitigated by the FNM cohesive elements, as the FNM formulation allows the cohesive elements to partition into SEs with respect to the matrix crack. In the FNM, the cohesive elements, when failing, join up with the matrix crack in a conforming manner, thereby reproducing the migration without introducing artefacts in 'A' and 'B' (Figure 15c).

6. Conclusions

In this work, the delamination migration phenomena in angle-ply laminates observed in the experiments by Pernice et al. [7] are studied numerically using the Floating Node Method (FNM). Complex phenomena such as the numerous kinking attempts and the multiple locations of migration across the width of the laminate are successfully predicted. The effect of load offset on the locations of migration is also captured. In addition, it is shown that, by using standard cohesive elements on the interface, one cannot capture migration, and that partitioning the interface cohesive element with respect to matrix cracks is critical for successfully predicting delamination migration.

7. Acknowledgement

The authors would like to acknowledge the research grant (No. R265000463112) from the Ministry of Education of Singapore and the Strategic Funding from National University of Singapore (No. R265000523646).

8. References

[1] J. G. Ratcliffe, M. W. Czabaj, T. K. O'Brien, A test for characterizing delamination migration in carbon/epoxy tape laminates, Tech. Rep., NASA, 2013.

[2] J. Rouchon, M. J. Bos, Fatigue and Damage Tolerance Evaluation of Structures: The Composite Materials Response, Tech. Rep., National Aerospace Laboratory, 2009.

[3] J. X. Tao, C. T. Sun, Influence of ply orientation on delamination in composite laminates, Journal of Composite Materials 32 (21) (1998) 1933–1947.

[4] E. S. Greenhalgh, C. Rogers, P. Robinson, Fractographic observations on delamination growth and the subsequent migration through the laminate, Composites Science and Technology 69 (14) (2009) 2345–2351.

[5] C. Canturri, E. S. Greenhalgh, S. T. Pinho, J. Ankersen, Delamination growth directionality and the subsequent migration processes–The key to damage tolerant design, Composites Part A: Applied Science and Manufacturing 54 (2013) 79–87.

[6] J. G. Ratcliffe, N. V. De Carvalho, Investigating delamination migration in composite tape laminates, Tech. Rep., NASA, 2014.

[7] M. F. Pernice, N. V. De Carvalho, J. G. Ratcliffe, S. R. Hallett, Experimental study on delamination migration in composite laminates, Composites Part A: Applied Science and Manufacturing 73 (2015) 20–34.

[8] N. V. De Carvalho, B. Y. Chen, S. T. Pinho, J. G. Ratcliffe, P. M. Baiz, T. E. Tay, Modeling delamination migration in cross-ply tape laminates, Composites Part A: Applied Science and Manufacturing 71 (2015) 192–203.

[9] L. Zhao, J. Zhi, J. Zhang, Z. Liu, N. Hu, XFEM simulation of delamination in composite laminates, Composites Part A: Applied Science and Manufacturing 80 (2016) 61–71.

[10] X. Li, J. Chen, An extended cohesive damage model for simulating multicrack propagation in fibre composites, Composite Structures 143 (2016) 1–8.

[11] M. McElroy, F. Leone, J. Ratcliffe, M. Czabaj, F. G. Yuan, Simulation of delamination–migration and core crushing in a CFRP sandwich structure, Composites Part A: Applied Science and Manufacturing 79 (2015) 192–202.

[12] T. E. Tay, X. S. Sun, V. B. C. Tan, Recent efforts toward modeling interactions of matrix cracks and delaminations: an integrated XFEM-CE approach, Advanced Composite Materials 23 (5-6) (2014) 391–408.

[13] X. F. Hu, B. Y. Chen, M. Tirvaudey, V. B. C. Tan, T. E. Tay, Integrated XFEM-CE analysis of delamination migration in multi-directional composite laminates, Composites Part A: Applied Science and Manufacturing 90 (2016) 161–173.

[14] B. Y. Chen, S. T. Pinho, N. V. De Carvalho, P. M. Baiz, T. E. Tay, A floating node method for the modelling of discontinuities in composites, Engineering Fracture Mechanics 127 (2014) 104 – 134.

[15] B. Y. Chen, T. E. Tay, S. T. Pinho, V. B. C. Tan, Modelling of the tensile failure of composites with the floating node method, Computer Methods in Applied Mechanics and Engineering 308 (2016) 414–442.

[16] A. Hansbo, P. Hansbo, A finite element method for the simulation of strong and weak discontinuities in solid mechanics, Computer Methods in Applied Mechanics and Engineering 193 (33-35) (2004) 3523–3540.

[17] J. Mergheim, E. Kuhl, P. Steinmann, A finite element method for the computational modelling of cohesive cracks, International Journal for Numerical Methods in Engineering 63 (2) (2005) 276–289.

[18] J.-H. Song, P. M. A. Areias, T. Belytschko, A method for dynamic crack and shear band propagation

with phantom nodes, International Journal for Numerical Methods in Engineering 67 (6) (2006) 868–893.

[19] T. Rabczuk, G. Zi, A. Gerstenberger, W. A. Wall, A new crack tip element for the phantom-node method with arbitrary cohesive cracks, International Journal for Numerical Methods in Engineering 75 (5) (2008) 577–599.

[20] F. P. van der Meer, L. J. Sluys, A phantom node formulation with mixed mode cohesive law for splitting in laminates, International Journal of Fracture 158 (2) (2009) 107–124.

[21] D. S. Ling, Q. D. Yang, B. Cox, An augmented finite element method for modeling arbitrary discontinuities in composite materials, International Journal of Fracture 156 (1) (2009) 53–73.

[22] X. J. Fang, Q. D. Yang, B. N. Cox, Z. Q. Zhou, An augmented cohesive zone element for arbitrary crack coalescence and bifurcation in heterogeneous materials, International Journal for Numerical Methods in Engineering 88 (2011) 841–861.

[23] T. Belytschko, Y. Y. Lu, L. Gu, Element-free Galerkin methods, International Journal for Numerical Methods in Engineering 37 (2) (1994) 229–256.

[24] W. K. Liu, S. Jun, Y. F. Zhang, Reproducing kernel particle methods, International Journal for Numerical Methods in Fluids 20 (8-9) (1995) 1081–1106.

[25] T. Rabczuk, S. Bordas, G. Zi, A three-dimensional meshfree method for continuous multiple-crack initiation, propagation and junction in statics and dynamics, Computational Mechanics 40 (3) (2007) 473–495.

[26] S. Bordas, T. Rabczuk, G. Zi, Three-dimensional crack initiation, propagation, branching and junction in non-linear materials by an extended meshfree method without asymptotic enrichment, Engineering Fracture Mechanics 75 (5) (2008) 943–960.

[27] I. Guiamatsia, B. Falzon, G. Davies, L. Iannucci, Element-free Galerkin modelling of composite damage, Composites Science and Technology 69 (15) (2009) 2640–2648.

[28] T. Belytschko, T. Black, Elastic crack growth in finite elements with minimal remeshing, International Journal for Numerical Methods in Engineering 45 (5) (1999) 601–620.

[29] N. Moës, J. Dolbow, T. Belytschko, A finite element method for crack growth without remeshing, International Journal for Numerical Methods in Engineering 46 (1) (1999) 131–150.

[30] G. N. Wells, L. J. Sluys, A new method for modelling cohesive cracks using finite elements, International Journal for Numerical Methods in Engineering 50 (12) (2001) 2667–2682.

[31] X. S. Sun, V. B. C. Tan, G. Liu, T. E. Tay, An enriched element-failure method (REFM) for delam-

ination analysis of composite structures, International Journal for Numerical Methods in Engineering 79 (6) (2009) 639–666.

[32] E. V. Iarve, M. R. Gurvich, D. H. Mollenhauer, C. A. Rose, C. G. Dávila, Mesh-independent matrix cracking and delamination modeling in laminated composites, International Journal for Numerical Methods in Engineering 88 (8) (2011) 749–773.

[33] T. Nagashima, H. Suemasu, X-FEM analyses of a thin-walled composite shell structure with a delamination, Computers & Structures 88 (9-10) (2010) 549–557.

[34] G. Francfort, J.-J. Marigo, Revisiting brittle fracture as an energy minimization problem, Journal of the Mechanics and Physics of Solids 46 (8) (1998) 1319 – 1342.

[35] B. Bourdin, G. A. Francfort, J.-J. Marigo, The Variational Approach to Fracture, Journal of Elasticity 91 (1-3) (2008) 5–148.

[36] C. Miehe, M. Hofacker, F. Welschinger, A phase field model for rate-independent crack propagation: Robust algorithmic implementation based on operator splits, Computer Methods in Applied Mechanics and Engineering 199 (2010) 2765 – 2778.

[37] M. J. Borden, C. V. Verhoosel, M. A. Scott, T. J. Hughes, C. M. Landis, A phase-field description of dynamic brittle fracture, Computer Methods in Applied Mechanics and Engineering 217 - 220 (2012) 77 – 95.

[38] N. Moës, C. Stolz, P.-E. Bernard, N. Chevaugeon, A level set based model for damage growth: the thick level set approach, International Journal for Numerical Methods in Engineering 86 (3) (2011) 358–380.

[39] P.-E. Bernard, N. Moës, N. Chevaugeon, Damage growth modeling using the Thick Level Set (TLS) approach: Efficient discretization for quasi-static loadings, Computer Methods in Applied Mechanics and Engineering 233 (2012) 11–27.

[40] C. Stolz, N. Moës, A new model of damage: a moving thick layer approach, International Journal of Fracture 174 (1) (2012) 49–60.

[41] F. P. van der Meer, L. J. Sluys, The thick level set method: sliding deformations and damage initiation, Computer Methods in Applied Mechanics and Engineering 285 (2015) 64–82.

[42] P. P. Camanho, C. G. Dávila, M. F. de Moura, Numerical simulation of mixed-mode progressive delamination in composite materials, Journal of Composite Materials 37 (16) (2003) 1415–1438.

[43] Q. D. Yang, B. Cox, Cohesive models for damage evolution in laminated composites, International Journal of Fracture 133 (2) (2005) 107–137.

[44] S. T. Pinho, L. Iannucci, P. Robinson, Formulation and implementation of decohesion elements in an explicit finite element code, Composites Part A-Applied Science and Manufacturing 37 (5) (2006) 778–789.

[45] G. Alfano, On the influence of the shape of the interface law on the application of cohesive-zone models, Composites Science and Technology 66 (6) (2006) 723–730.

[46] A. Turon, C. G. Dávila, P. P. Camanho, J. Costa, An engineering solution for mesh size effects in the simulation of delamination using cohesive zone models, Engineering Fracture Mechanics 74 (10) (2007) 1665–1682.

[47] P. W. Harper, S. R. Hallett, Cohesive zone length in numerical simulations of composite delamination, Engineering Fracture Mechanics 75 (16) (2008) 4774–4792.

[48] M. R. Wisnom, Modelling discrete failures in composites with interface elements, Composites Part A-Applied Science and Manufacturing 41 (7) (2010) 795–805.

[49] F. P. van der Meer, L. J. Sluys, S. R. Hallett, M. R. Wisnom, Computational modeling of complex failure mechanisms in laminates, Journal of Composite Materials 46 (5) (2012) 603–623.

[50] B. Y. Chen, T. E. Tay, P. M. Baiz, S. T. Pinho, Numerical analysis of size effects on open-hole tensile composite laminates, Composites Part A: Applied Science and Manufacturing 47 (0) (2013) 52 – 62.

[51] M. Ridha, C. Wang, B. Chen, T. Tay, Modelling complex progressive failure in notched composite laminates with varying sizes and stacking sequences, Composites Part A: Applied Science and Manufacturing 58 (2014) 16–23.

[52] Z. C. Su, T. E. Tay, M. Ridha, B. Y. Chen, Progressive damage modeling of open-hole composite laminates under compression, Composite Structures 122 (2015) 507–517.